Vibrational contributions to the phase stability of PbS-PbTe alloys

Jeff W. Doak, C. Wolverton, and Vidvuds Ozoliņš

Phys. Rev. B **92**, 174306 — Published 30 November 2015

DOI: 10.1103/PhysRevB.92.174306

Vibrational contributions to the phase stability of PbS–PbTe alloys

Jeff W. Doak and C. Wolverton*

Department of Materials Science and Engineering,

Northwestern University, Evanston, Illinois 60208, USA

Vidvuds Ozoliņš

Department of Materials Science and Engineering,

University of California, Los Angeles, California 90095, USA

(Dated: November 4, 2015)

Abstract

The thermoelectric figure of merit (ZT) of semiconductors such as PbTe can be improved by forming nanostructures within the bulk of these materials. Alloying PbTe with PbS causes PbS-rich nanostructures to precipitate from the solid solution, scattering phonons and increasing ZT. Understanding the thermodynamics of this process is crucial to optimizing the efficiency gains of this technique. Previous calculations of the thermodynamics of PbS–PbTe alloys [(J. W. Doak and C. Wolverton, Phys. Rev. B 86, 144202 (2012)] found that mixing energetics alone were not sufficient to quantitatively explain the thermodynamic driving force for phase separation in these materials: first-principles calculations of the thermodynamics of phase separation over-estimate the thermodynamic driving force for precipitation of PbS-rich nanostructures from PbS–PbTe alloys. In this work, we re-examine the thermodynamics of PbS–PbTe, including the effects of vibrational entropy in the free energy through frozen-phonon calculations of special quasirandom structures (SQS) to explain this discrepancy between first-principles and experimental phase stability. We find that vibrational entropy of mixing reduces the calculated maximum miscibility gap temperature T_G of PbS–PbTe by 470 K, bringing the error between calculated and experimental T_G down from 700 K to 230 K. Our calculated vibrational spectra of PbS–PbTe SQS exhibit dynamic instabilities of S ions which corroborate reports of low-T ferroelectric-like phase transitions in solid solutions of PbS and PbTe which are not present in either of the constituent compounds. We use our calculated vibrational spectra to obtain phase transition temperatures which are in qualitative agreement with experimental results for PbTe-rich alloys, as well as to predict the existence of a low-T displacive phase transition in PbS-rich PbS–PbTe which has not yet been experimentally investigated.

I. INTRODUCTION

Nanostructures formed within a bulk matrix material have been used to improve the thermoelectric figure of merit, $ZT = TS^2\sigma/(\kappa_l + \kappa_e)$, of a variety of semiconductor alloy systems, including the prototypical system PbS–PbTe.[1–8] These nanostructures increase ZT by reducing the lattice thermal conductivity, κ_l, of the alloy without overly affecting the electronic thermal conductivity, κ_e, or other electronic transport properties (electrical conductivity σ or Seebeck coefficient S).[9,10] In certain systems, such as PbSe–CdSe, PbSe–ZnSe[5] SnTe–CdTe,[7] or SnTe–HgTe,[8] the alloying element can play a ZT-enhancing role in the matrix phase in addition to forming nanostructures; Cd and Zn in PbSe and Cd and Hg in SnTe all reduce the energy separation between the two highest-lying maxima in the valence band of the host phase (at L and Σ in the rocksalt BZ, respectively), increasing the Seebeck coefficient.

Optimizing the phase separation process which gives rise to nanostructures requires understanding the thermodynamics of phase separation in these systems: the free energy of mixing as a function of composition and temperature. The experimentally-determined phase diagram of PbS–PbTe[11,12] contains a miscibility gap—a region of compositions where a solid-solution of PbS and PbTe will thermodynamically prefer separation into a PbS-rich phase and a PbTe-rich phase. Nanostructures in PbS–PbTe are formed using this miscibility gap: cooling an alloy of PbS–PbTe from a temperature above the miscibility gap (where the alloy is a solid solution) down to a temperature within the gap causes a PbS-rich nanostructured phase to form from the PbTe-rich matrix.[1,9,10,13]

Previous first-principles calculations of the thermodynamics of PbS–PbTe showed that while density functional theory (DFT) energetics capture the asymmetry of the equilibrium miscibility gap in composition, the calculated temperatures of the miscibility gap are in poor agreement with experiment.[14] In particular, the maximum temperature of the miscibility gap T_{G} has been calculated to be 1770 K,[14] approximately a 65% error with respect to the measured maximum miscibility gap temperature of 1070 K.[11,12] These thermodynamic calculations were based on a mean-field model of mixing that included only a temperature-independent mixing energy (fit to DFT energetics) and an ideal configurational entropy (for mixing S and Te on the anion fcc sublattice of the rocksalt structure),

$$\Delta F_{\mathrm{mix}}(x,T) = \Delta E_{\mathrm{mix}}(x) - T\Delta S^{\mathrm{ideal}}_{\mathrm{mix}}(x) \tag{1}$$

The failure of this free energy of mixing to capture the correct solid-state phase diagram of PbS–PbTe suggests that important physical contributions to the free energy are missing from the above model.

There are several possible contributions to the free energy of mixing which could be significant. These include the magnetic entropy of mixing,[15] electronic entropy of mixing,[16] non-ideal configurational entropy,[17] and vibrational entropy of mixing.[18] Of these, the magnetic entropy of mixing should be negligible because these systems are non-magnetic, the electronic entropy of mixing should be small due to the semiconducting nature of the pure compounds PbS and PbTe as well as their solid solution, and the non-ideal configurational entropy should also play a small role due to the dominance of the long-range strain interactions[19] in previously calculated mixing energetics.[14] In contrast, the vibrational entropy of mixing can have a potentially significant effect on the phase stability of an alloy system.[17,18,20–24]

In alloy systems where the constituent compounds have a large lattice mismatch (PbS and PbTe have a lattice mismatch of 8.5%[25,26]), the vibrational entropy of mixing has been attributed to a size-mismatch effect.[21,23] The size-mismatch effect posits that when the constituent atoms of an alloy have large size differences, the disordered alloy will, by necessity, contain regions that are locally in compression or tension resulting in stiffer or weaker bonds, respectively. The magnitude and sign of the size-mismatch effect (i.e. stabilizing vs. destabilizing the disordered phase relative to the phase-separated constituents) then depends on the details of the atomic relaxations in the disordered alloy. This size-mismatch effect may be heightened by the inherently anharmonic nature of the bonds in the lead chalcogenides,[27–36] whose anharmonicity is due to the resonant, half-filled p-states shared by the six nearest-neighbor (NN) chalcogen anions of each Pb cation.[37] Finally, there is some experimental evidence that PbS–PbTe alloys undergo a ferroelectric-like phase transition at very low temperatures, even though neither constituent compound is a ferroelectric.[38–42] This transition has been attributed to off-center S ions in the PbS–PbTe solid solution forming local dipole moments which undergo order-disorder and/or displacive transitions depending on S concentration,[38,39,42] similar to other off-center ions,[43,44] dipole glasses,[45] and possibly relaxors.[46] The physics of S-ion dipole-moment ordering falls within the lattice dynamics of PbS–PbTe and so could play a role in the vibrational entropy of mixing, even at temperatures above a ferroelectric phase transition.

In this work, we investigate the effect of vibrational entropy on the thermodynam-

ics of mixing in PbS–PbTe using first-principles DFT[47,48] calculations of the vibrational spectra of special quasirandom structures (SQS)[49,50]—structures which approximate the random alloy of PbS–PbTe. DFT calculations have been used to study the vibrational properties[29,30,32,35,36,51–55] and phase stability of thermoelectric systems.[14,56–60] DFT calculations have also been used to study phase separation processes in a variety of materials systems,[17,61–63] in some cases including the effects of vibrational entropy.[20,64–66] In Sec. II we describe the theoretical framework for our calculations and the computational methodology used to carry them out. In Sec. III we discuss the vibrational and thermodynamic properties of PbS–PbTe SQS, the effect of local relaxations on the atomic-scale structural properties of PbS–PbTe SQS, and construct a solid-state phase diagram of PbS–PbTe which incorporates the effects of vibrational entropy.

We find that PbTe-rich PbS–PbTe alloys have complex energy landscapes with shallow barriers, giving rise to soft phonon modes. These phonon modes correspond to displacements of S ions, supporting the hypothesis of off-center S ions in the random alloy at low temperatures. We also find that Pb ions are statically displaced from their ideal lattice sites to accommodate the lattice mismatch between PbS and PbTe in the solid solution, in contrast to the anion sublattice which largely retains its ideal lattice arrangement. Using a mean-field model of phase transitions in a soft-mode ferroelectric,[67] we calculate the displacive transition temperatures of PbS–PbTe SQS and find them to be in good qualitative agreement with experimentally measured phase-transition temperatures. Finally, we find that the vibrational entropy of mixing reduces the temperatures of the previously-calculated miscibility gap in PbS–PbTe by 470 K, bringing the DFT-calculated phase diagram into much better agreement with the experimentally measured diagram and reducing the percent error relative to experiment to 21%.

II. METHODOLOGY

A. Atomic-scale model of random alloys

To study the composition and temperature dependence of a solid solution of PbS and PbTe with atomistic computational techniques, we need a model of the atomic-scale structure of a random alloy within the periodic boundary conditions employed by plane-wave

electronic structure calculations. Because, we expect the effects of local atomic relaxations due to differing nearest-neighbor coordination to play a large role in the vibrational spectra of an alloy,[21] capturing these effects in our atomic model of the random alloy is important. The method of SQS[49,50] provides an approximate model of the random alloy that allows for atomic relaxations and is well suited to our needs.

A special quasirandom structure is a small supercell of the parent lattice with mixing atoms placed on each lattice site in such a way that the correlation functions of the supercell closely approximate the short-range correlation functions of a perfectly random alloy at the same composition. Typically-considered correlation functions are pairs out to some distance and triplets out to a smaller distance.

In this work we consider mixing on the anion sublattice of the rocksalt crystal structure. The anion sublattice is an fcc lattice, so we can take existing fcc SQS-16 structures[68] and add in the spectator cation sublattice, which gives us 32-atom rocksalt SQS. In addition, we have created 27-mixing-atom SQS (54-atoms total) at compositions $x = 1/3$ and $x = 2/3$ with unit cells shaped like $3 \times 3 \times 3$ supercells of the rocksalt primitive cell, which are described in more detail in the appendix. Finally, to model dilute additions of S to PbTe or Te to PbS, we consider 54-atom $3 \times 3 \times 3$ supercells of PbS or PbTe with one anion replaced with Te or S, respectively. With these supercells, we can approximate the structure of a random alloy of PbS–PbTe at various compositions, which we use to calculate the composition and temperature dependence of the free energy of mixing as described in Secs. II B and II C.

B. Free energy of mixing

The free energy of mixing in a (pseudo-)binary random alloy, $\Delta F_{\text{mix}}(x,T)$, can be written as

$$\Delta F_{\text{mix}}(x,T) = \Delta E_{\text{mix}}(x,T) - T[\Delta S^{\text{ideal}}_{\text{mix}}(x) + \Delta S^{\text{xs}}_{\text{mix}}(x,T)], \tag{2}$$

where $\Delta S^{\text{ideal}}_{\text{mix}}(x)$ is the ideal, mean-field configurational entropy,

$$\Delta S^{\text{ideal}}_{\text{mix}}(x) = -k_B \left[x \ln x + (1-x)\ln(1-x)\right], \tag{3}$$

$\Delta E_{\text{mix}}(x,T)$ is a mixing energy, and $\Delta S^{\text{xs}}_{\text{mix}}(x,T)$ is an excess mixing entropy. The mixing energy and excess mixing entropy terms can be composed of several different contributions: (i) a concentration-dependent zero Kelvin mixing energy $\Delta E^{\text{0K}}_{\text{mix}}(x)$ and associated with it a

non-ideal configurational entropy $\Delta S^{\text{xs}}_{\text{config}}(x)$, (ii) the energy and entropy of electronic excitations $\Delta E^{\text{el}}_{\text{mix}}(x,T)$ and $\Delta S^{\text{el}}_{\text{mix}}(x,T)$, (iii) the energy and entropy of magnetic configurations $\Delta E^{\text{mag}}_{\text{mix}}(x,T)$ and $\Delta S^{\text{mag}}_{\text{mix}}(x,T)$, and (iv) the energy and entropy of vibrational excitations $\Delta E^{\text{vib}}_{\text{mix}}(x,T)$ and $\Delta S^{\text{vib}}_{\text{mix}}(x,T)$. Of these four contributions to the excess free energy of mixing, we expect terms (i) and (iv) to play the largest role in PbS–PbTe. Terms (ii) and (iii) should be negligible due to the semiconducting and non-magnetic nature of the material. In addition, the dominant contributions to $\Delta E^{\text{0K}}_{\text{mix}}(x)$ come from long-range strain effects,[14] which tend to make the excess configurational entropy less important than the ideal configurational entropy.[19] Finally, as will be discussed in Sec. II C, the vibrational energy of mixing is approximately zero above room temperature and all of the effects of vibrations on the thermodynamics of mixing are due to a largely T-independent vibrational entropy of mixing. Based on these considerations, we can approximate the free energy of mixing as

$$\Delta F_{\text{mix}}(x,T) \approx \Delta E^{\text{0K}}_{\text{mix}}(x) - T[\Delta S^{\text{ideal}}_{\text{mix}}(x) + \Delta S^{\text{vib}}_{\text{mix}}(x)]. \tag{4}$$

To model the composition dependence of $\Delta E^{\text{0K}}_{\text{mix}}(x)$ and $\Delta S^{\text{vib}}_{\text{mix}}(x)$ we continue to use the mean-field approach and approximate each function as a solution model based on Redlich-Kister (RK) polynomials.[69] These solution models take the form

$$\Delta Q^{k}_{\text{mix}}(x) = x(1-x)\left[\sum_{i=0}^{k} L_i(1-2x)^i\right] \tag{5}$$

where $\Delta Q^{k}_{\text{mix}}$ is an excess-mixing quantity, k is the order of the solution model ($k = 0$, 1, and 2 are called regular, subregular, and subsubregular solution models, respectively), and L_i are quantity-dependent parameters which are fit to DFT-calculated data as described in Sec. III B. Assuming a subregular solution model form for both $\Delta E^{\text{0K}}_{\text{mix}}(x)$ and $\Delta S^{\text{vib}}_{\text{mix}}(x)$, this approach gives us an analytical free energy of mixing which can be expressed as

$$\Delta F_{\text{mix}}(x,T) = x(1-x)[(L_0^{\text{0K}} - TL_0^{\text{vib}}) + (L_1^{\text{0K}} - TL_1^{\text{vib}})(1-2x)] + k_B T[x\ln x + (1-x)\ln(1-x)], \tag{6}$$

and from this free energy we can calculate the solvus boundaries of PbS–PbTe.

The equilibrium phase diagram of an alloy system can be determined from a common-tangent construction, where the chemical potentials of each chemical species are the same in every phase coexisting in equilibrium. We treat PbS and PbTe as the chemical species

in the pseudo-binary system PbS–PbTe. For a system which thermodynamically separates into two different phases α and β, we can write the free energy of each phase $\Delta F^{\alpha}_{\rm mix}$ and $\Delta F^{\beta}_{\rm mix}$ as the free energy in Eq. (6) with different compositions, x_α and x_β. We can then determine the equilibrium values of these compositions at a given temperature T by solving the system of equations

$$\frac{\partial}{\partial x_\alpha}\Delta F^{\alpha}_{\rm mix}(x_\alpha,T)=\frac{\partial}{\partial x_\beta}\Delta F^{\beta}_{\rm mix}(x_\beta,T)=\frac{\Delta F^{\beta}_{\rm mix}(x_\beta,T)-\Delta F^{\alpha}_{\rm mix}(x_\alpha,T)}{x_\beta-x_\alpha}. \tag{7}$$

The miscibility gap calculated from Eq. (7) has a chemical spinodal $T_{\rm sp}(x)$, defined by $\frac{\partial^2}{\partial x^2}\Delta F_{\rm mix}(x,T)=0$. The maximum miscibility gap temperature T_G occurs where $\frac{d}{dx}T_{\rm sp}=0$. For the functional form given by Eq. (6), $T_{\rm sp}$ can be written as

$$T_{\rm sp}=\frac{x(1-x)[2L_0^{\rm 0K}+6L_1^{\rm 0K}(1-2x)]}{k_B+x(1-x)[2L_0^{\rm vib}+6L_1^{\rm vib}(1-2x)]}. \tag{8}$$

C. Vibrational thermodynamics

The vibrational free energy of a compound in the harmonic approximation can be obtained from the phonon density of states (DOS) $g(\nu)$ by[20,70]

$$F^{\rm vib}=k_BT\int_0^\infty g(\nu)\ln\left[2\sinh\frac{h\nu}{2k_BT}\right]d\nu. \tag{9}$$

At high temperatures (above the Debye temperature of the material), the vibrational energy of a compound $E^{\rm vib}$ is equal to $3k_BT$. The vibrational free energy of *mixing* at high temperatures is therefore only due to the vibrational entropy of mixing. In the high-T limit, the vibrational entropy of mixing $\Delta S^{\rm vib}_{\rm mix}$ is temperature independent and given by

$$\Delta S^{\rm vib}_{\rm mix}(x)=-k_B\int_0^\infty \Delta g(\nu,x)\ln(\nu)d\nu, \tag{10}$$

where the phonon DOS of mixing $\Delta g(\nu,x)$ is

$$\Delta g(\nu,x)=g_{A(B_{1-x}C_x)}(\nu)-(1-x)g_{AB}(\nu)-xg_{AC}(\nu), \tag{11}$$

and $g_{A(B_{1-x}C_x)}$, g_{AB}, and g_{AC} are the phonon densities of states for a pseudo-binary solid solution and constituent compounds, respectively.

D. Low-T phase transitions

To model the low-T thermodynamics of a soft-mode ferroelectric system (as has been proposed for the PbS–PbTe solid solution[38,39]), we follow Ref. 67 and consider a system with an unstable phonon mode leading to a double-well potential energy, $V(\phi) = -\frac{1}{2}\kappa_2\phi^2 + \frac{1}{4}\kappa_4\phi^4$, as a function of the soft-mode normal coordinate ϕ. The high-T phase exists at $\phi = 0$, while the low-T phase exists at non-zero ϕ. We can define a Hamiltonian for the high-T phase which a potential energy contribution composed of (i) the soft-mode potential energy, (ii) a summation over the stable phonon modes, and (iii) an anharmonic coupling between the stable phonon modes and the soft-mode normal coordinate:[67]

$$\mathcal{H} = V(\phi) + \frac{1}{2}\sum_i \nu_i^2 Q_i^2 + \frac{1}{4}\sum_i \alpha_i \phi^2 Q_i^2, \tag{12}$$

where Q_i is the normal coordinate of phonon mode i, ν_i is the frequency of mode i, and α_i is anharmonic coupling constant for mode i. This Hamiltonian can be rewritten as a pseudo-harmonic Hamiltonian to renormalize the phonon frequencies in the low-T phase. These renormalized phonon frequencies are given by[67]

$$\tilde{\nu}_i^2(\phi) = \nu_i^2 + \frac{1}{2}\alpha_i\phi^2. \tag{13}$$

We can use Eq. (13) along with DFT-calculated Γ-point phonon frequencies of the dynamically-unstable high-T phase and stabilized low-T phase to determine, at least qualitatively, the anharmonic coupling parameters α_i. The bare frequencies ν_i come directly from the harmonic frequencies of the dynamically-unstable high-T phase. At the maximum value of the unstable mode displacement $\phi_{\max}$, the system is in the geometric configuration of the low-T phase. We find the renormalized harmonic frequencies at this value of the soft-mode displacement $\tilde{\nu}_i(\phi_{\max})$ using the dynamical matrix of the system in the low-T phase, $\mathbf{D}_{\mathrm{LT}}$. Because the normal modes of the low-T and high-T phases do not correspond exactly to one another, we approximate $\tilde{\nu}_i^2(\phi_{\max})$ as the effective squared phonon frequencies of the low-T phase along directions corresponding to the normal mode displacements of the high-T phase, $|e_i\rangle$:

$$\tilde{\nu}_i^2(\phi_{\max}) \approx \langle e_i | \, \mathbf{D}_{\mathrm{LT}} \, | e_i \rangle \, . \tag{14}$$

Inserting Eq. (14) into Eq. (13) at $\phi = \phi_{\max}$ and solving for α_i, we find

$$\alpha_i = \frac{2}{\phi_{\max}^2}\left(\langle e_i | \, \mathbf{D}_{\mathrm{LT}} \, | e_i \rangle - \nu_i^2 \right). \tag{15}$$

Once the anharmonic coupling constants have been determined using Eq. (15), we can use the Hamiltonian defined in Eq. (12) to define a vibrational free energy for the system,[67]

$$F(\phi, T) = V(\phi) + k_B T \sum_i \ln \left[2 \sinh \frac{h\tilde{\nu}_i(\phi)}{2k_B T} \right], \tag{16}$$

which we can minimize with respect to ϕ as a function of T to find $\phi(T)$ and T_c, the temperature at which $\phi \to 0$ and the system undergoes a phase transition between the low- and high-T phases.

E. Computational methodology

Structural relaxations and finite-displacement phonon calculations were performed within DFT using the Vienna *Ab-initio* Simulation Package (VASP)[71–74]. All calculations were performed with projector augmented wave (PAW)[75,76] potentials and the generalized gradient approximation (GGA) of Perdew, Burke, and Ernzerhof (PBE)[77] for the exchange-correlation functional. The potentials used had the $6s^2 6p^2$, $3s^2 3p^4$, and $5s^2 5p^4$ electrons as valence for Pb, S, and Te, respectively. Spin-orbit interactions have been found to have minimal effect ($\sim 0.1\%$) on the lattice constants of the lead chalcogenides[52] and require significant computational expense, therefore we do not include them in our calculations.

Structural relaxations were carried out on 54-atom, $3 \times 3 \times 3$ supercells of pure PbS and PbTe as well as the SQS described in Sec. II A using 500 eV energy cutoffs Monkhorst-Pack (MP) k-point meshes[78] with 5000 k-points per reciprocal atom (KPPRA) ($8 \times 6 \times 4$ meshes for SQS-16 cells and $6 \times 6 \times 6$ meshes for SQS-27, dilute-impurity, and pure $3 \times 3 \times 3$ supercells), and Gaussian smearing of electronic occupations with a 0.1 eV smearing width. To ensure accurate forces during the relaxation, calculations were performed with "high" precision, an additional support grid was added to increase the accuracy of the calculation of augmentation charges, and self-consistent cycles were iterated until changes in the electronic energy were less than 10^{-8} eV. Ionic relaxations were carried out with a quasi-Newton algorithm[79] to minimize the forces and stresses on each structure, with the relaxations occurring until forces were less than 10^{-3} eV/Å. To ensure accurate relaxations and energies, for each structure two relaxations were performed, followed by a static calculation.

Frozen phonon calculations were performed for each fully relaxed structure using the methodology of Ref. 80. Each inequivalent atom was displaced along symmetrically distinct

directions in a ballistic trajectory [using constant-velocity molecular dynamics (MD)] consisting of 5 evenly distributed displacements from −0.6 Å to +0.6 Å centered around the equilibrium position. The dynamical matrix was fit to the resulting forces, which was then diagonalized to obtain phonon mode eigenvectors and eigenvalues. Force constant matrices were calculated by reverse Fourier transforming the dynamical matrices, and phonon DOSs were obtained by extrapolating the force constant matrix onto $10 \times 10 \times 10$ q-point meshes and calculating phonon frequencies, which were broadened using Gaussian peaks with 1 cm^{-1} broadening widths.

Due to a relaxation criteria of zero forces instead of a minimized energy, some SQS and dilute-defect calculations relaxed to saddle-points in their energy landscapes, resulting in imaginary phonon modes. For these structures, energy vs. phonon mode displacement calculations were performed to identify the minimum-energy wells neighboring the saddle-points. These structures were moved to these minimum-energy configurations, and damped-MD relaxations were performed to relax the structures within these wells. Once the structures were re-relaxed, finite-displacement phonon calculations were performed.

III. RESULTS AND DISCUSSION

A. Vibrational properties of PbS–PbTe solid solutions

We first present the results of our frozen-phonon calculations for PbS, PbTe, and PbS–PbTe SQS with compositions $x_{\mathrm{PbTe}} = 1/27$, $x_{\mathrm{PbTe}} = 1/4$, $x_{\mathrm{PbTe}} = 1/3$, $x_{\mathrm{PbTe}} = 1/2$, $x_{\mathrm{PbTe}} = 2/3$, $x_{\mathrm{PbTe}} = 3/4$, and $x_{\mathrm{PbTe}} = 26/27$. Quasi-Newton force relaxations of several SQS relaxed the structures to low-energy saddle-points of the energy landscape rather than energy minima. Γ-point frozen phonon calculations of these systems gave harmonic phonon modes with imaginary frequencies. The systems with these dynamical instabilities, and their imaginary-mode frequencies are shown in Table I. To better understand the complexity of the energy landscapes of these PbS–PbTe alloys, we plot the unstable phonon-mode trajectories of these 'saddle-point' structures in Fig. 1. The energy landscapes of these unstable phonon modes all correspond to double-well structures with the relaxed structure lying at the saddle-point of the double well. The double-well structures have energy barriers of 1.6, 0.41, 0.40, and 0.11 meV/cation, respectively.

TABLE I. List of SQS compositions of PbS–PbTe alloys with unstable phonon modes. Imaginary mode frequencies are given as positive numbers.

x_{PbTe}	$\nu \times (-i)$ (cm^{-1})		
1/3	51.11	48.16	46.88
	42.97	41.40	35.68
	33.43	31.81	
1/2		14.21	
2/3		33.08	
3/4		35.05	
26/27	24.01	24.01	24.01

Insets in each panel of Fig. 1 show the atomic displacements corresponding to the energy wells of each structure. The displacements of the $x_{\mathrm{PbTe}} = 1/3$ structure consist of eight S ions (out of 27 anions) moving along their 1st NN Pb–S bonds or in between two Pb–S bonds. The displacements of the $x_{\mathrm{PbTe}} = 2/3$ structure consist of two S ions (out of 27 anions) oriented linearly in chain moving along that line. Similarly, the displacements of the $x_{\mathrm{PbTe}} = 3/4$ structure consist of one S ion and one neighboring Pb ion moving in opposite directions along their connecting bond. Finally, the displacements of the $x_{\mathrm{PbTe}} = 26/27$ structure consist of the single S ion and two opposing Pb NN ions moving along their connecting bonds.

Displacement of the $x_{\mathrm{PbTe}} = 1/3$ and $x_{\mathrm{PbTe}} = 2/3$ SQS along their unstable mode trajectories and subsequent relaxations resulted in Γ-point harmonic phonon modes that were all stable. The total phonon DOS (g) of these re-relaxed structures, as well as the other systems with stable phonon modes are presented in Fig. 2, along with the composition-weighted sum of the phonon DOSs of PbS and PbTe $[xg_{\mathrm{PbTe}} + (1-x)g_{\mathrm{PbS}}]$ and the phonon DOS of mixing Δg. We also compare our calculated phonon DOSs for PbS and PbTe with phonon DOSs derived from experimental neutron diffraction data[81,82] in Fig. 2 and find the DFT-calculated phonon DOSs give good agreement with the experimentally-derived DOSs.

To obtain the vibrational entropy of mixing, $\Delta S^{\mathrm{vib}}_{\mathrm{mix}}$, for the dynamically stable PbS–PbTe SQS, we calculate the logarithmic moment of the phonon DOS of mixing Δg shown in Fig. 2 using Eq. (10). The resulting vibrational entropies of mixing are provided in Table II

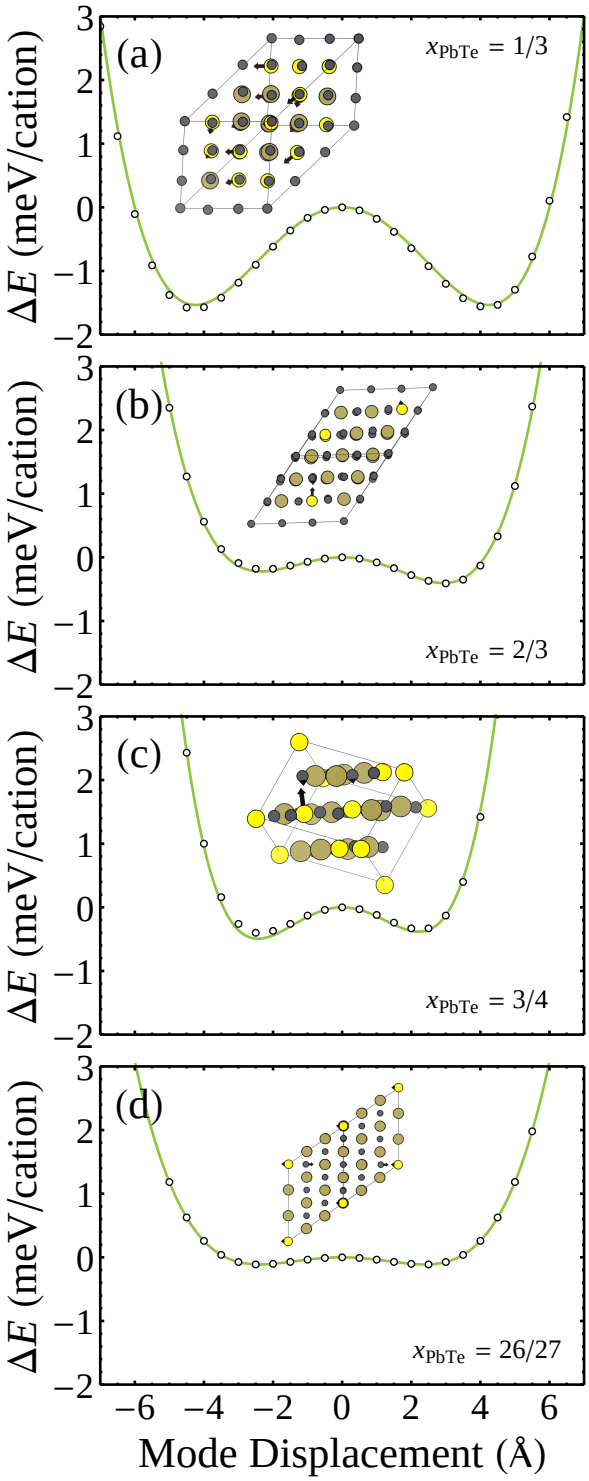

FIG. 1. (Color online) Energy vs. imaginary normal-mode coordinate for PbS–PbTe SQS with compositions (a) $x_{PbTe} = 1/3$, (b) $x_{PbTe} = 2/3$, and (c) $x_{PbTe} = 3/4$, and (d) $x_{PbTe} = 26/27$. Data points are DFT-calculated energies and curves are polynomial fits to data. Insets show atomistic models of SQS (Pb atoms in gray, S atoms in yellow, and Te atoms in brown) with atomic displacement vectors corresponding to each normal mode. These double-well potential energy landscapes have barrier heights of 1.6, 0.41, 0.40, and 0.11 meV/cation, respectively.

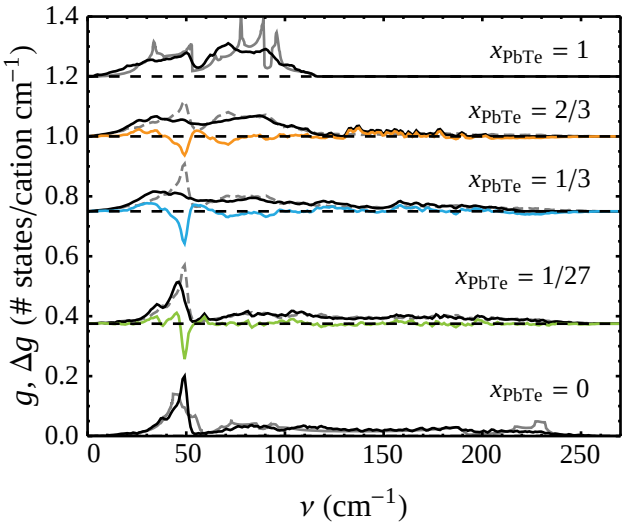

FIG. 2. (Color online) Phonon DOS of mixing for PbS–PbTe SQS. Total phonon DOSs (g) for each SQS are shown as solid black lines. Composition-weighted averages of the phonon DOS of PbS and PbTe $[xg_{\mathrm{PbTe}} + (1-x)g_{\mathrm{PbS}}]$ are shown at each SQS composition as dashed gray lines. The difference between these curves, the phonon DOS of mixing (Δg), defined in Eq. (11), are shown as solid colored lines for 54-atom SQS with stable phonon modes. Phonon DOSs derived from experimental neutron-diffraction data for PbS[82] and PbTe[81] are shown as solid gray lines. Each phonon-DOS is offset along the vertical axis for clarity; dashed lines indicate the zero for each phonon-DOS.

TABLE II. Vibrational entropies of mixing, $\Delta S_{\mathrm{mix}}^{\mathrm{vib}}$ of PbS–PbTe solid solutions obtained from $\Delta g(\nu)$ using Eq. (10). For comparison, values of the ideal configurational entropy of mixing [Eq. (3)] are shown at the same compositions.

x_{PbTe}	$\Delta S_{\mathrm{mix}}^{\mathrm{vib}}$ (k_{B}/cation)	$\Delta S_{\mathrm{mix}}^{\mathrm{ideal}}$ (k_{B}/cation)
1/27	0.10	0.16
1/3	0.17	0.64
2/3	0.22	0.64

along with the values of the ideal entropy of mixing at the same compositions. We find the vibrational entropies of mixing to be positive, favoring the solid solution over the phase-separated state. In Sec. III B we will consider the quantitative effects that the vibrational entropy of mixing has on the free energy of mixing and phase stability in PbS–PbTe alloys.

TABLE III. Sub-regular solution model parameters [Eq. (5)] for the mixing energy and vibrational entropy of mixing of PbS–PbTe solid solutions.

	L_0	L_1
$\Delta E_{\rm mix}^{\rm 0K}$ (meV/cation)	301.13	53.16
$\Delta S_{\rm mix}^{\rm vib}$ ($k_{\rm B}$/cation)	0.90	0

B. Contributions to the free energy of mixing in PbS–PbTe

To quantify the terms in the free energy of mixing [Eq. (6)], in Fig. 3 we plot the mixing energies $\Delta E_{\rm mix}^{\rm 0K}$ and vibrational entropies of mixing $-T\Delta S_{\rm mix}^{\rm vib}$ at $T = 700$ K for PbS–PbTe SQS as green and red data points, respectively. The PbS–PbTe SQS mixing energy is defined as

$$\Delta E_{\rm mix}^{\rm 0K}(x) = E_{\rm SQS}(x) - xE_{\rm PbTe} - (1-x)E_{\rm PbS}, \tag{17}$$

where $E_{\rm SQS}$, $E_{\rm PbS}$, and $E_{\rm PbTe}$ are the DFT total energies of the SQS, PbS, and PbTe, respectively. The mixing energies for $x_{\rm PbTe} = 1/4$, $1/2$, and $3/4$ are consistent with previously calculated values.[14] In Fig. 3 we also show least-squares fits of the RK polynomial solution model of Eq. (5) to the SQS mixing energies and SQS vibrational entropies of mixing as green and red lines, respectively. Shaded regions around each line are 90% confidence intervals for the least-squares fits. Figure 3 also shows the ideal mixing entropy [Eq. (3)] as $-T\Delta S_{\rm mix}^{\rm ideal}$ at $T = 700$ K as a blue line and the combined free energy of mixing $\Delta F_{\rm mix}$ [Eq. (6)] as a black line with the combined 90% confidence interval of $\Delta E_{\rm mix}^{\rm 0K}$ and $\Delta S_{\rm mix}^{\rm vib}$ shown as an estimate of the error of our free energy of mixing.

The least-squares fits to $\Delta E_{\rm mix}^{\rm 0K}$ and $\Delta S_{\rm mix}^{\rm vib}$ give R^2 values of 0.996 and 0.934, respectively. The solution model parameters corresponding to these fits are shown in Table III. The order of the solution model for each quantity is chosen based on a leave-one-out cross-validation (CV) comparison. The CV scores of solution models of order 0, 1, and 2 for $\Delta E_{\rm mix}^{\rm 0K}$ are 6.35, 5.22, and 6.12 meV/cation, respectively and for $\Delta S_{\rm mix}^{\rm vib}$ are 0.06, 0.35, and 0.11 k_B/cation, respectively. From this analysis we conclude that (i) while all three solution models are good predictors of PbS–PbTe SQS mixing energies, the subregular solution model (order 1) provides more predictive power than the other two models and (ii) the regular solution model (order 0) provides the best predictive power for PbS–PbTe SQS vibrational entropies

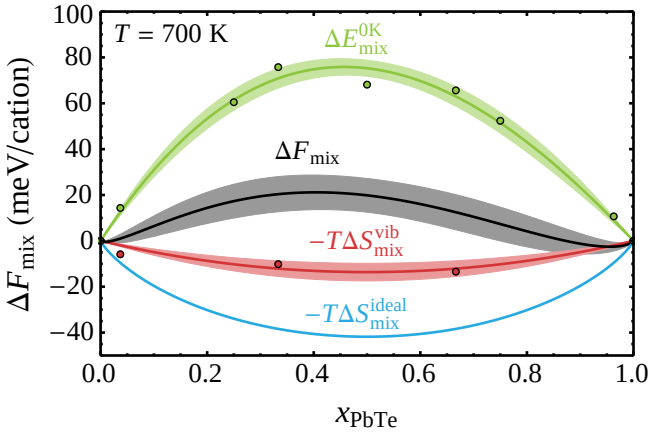

FIG. 3. (Color online) Contributions to the free energy of mixing ΔF_{mix} [Eq. (4)] at 700 K: zero Kelvin mixing energetics $\Delta E^{0\mathrm{K}}_{\mathrm{mix}}$ (green), vibrational entropy of mixing $-T\Delta S^{\mathrm{vib}}_{\mathrm{mix}}$ (red), and ideal entropy of mixing $-T\Delta S^{\mathrm{ideal}}_{\mathrm{mix}}$ (blue). Green data points and solid line show DFT-calculated energetics and a subregular solution model fit to this data, respectively. Red data points and solid line show vibrational entropies of mixing calculated from $\Delta g(\nu)$ and a regular solution model fit to this data, respectively. Shaded regions show 90% confidence intervals for fits to $\Delta E^{0\mathrm{K}}_{\mathrm{mix}}$, $\Delta S^{\mathrm{vib}}_{\mathrm{mix}}$, and their summed contribution to ΔF_{mix}.

of mixing. Thus we use RK polynomials of order 1 (subregular) and 0 (regular) to model $\Delta E^{0\mathrm{K}}_{\mathrm{mix}}$ and $\Delta S^{\mathrm{vib}}_{\mathrm{mix}}$, respectively.

C. Structural properties of PbS–PbTe SQS

In Figs. 4 and 5 we show the average (cubic) lattice parameter of PbS–PbTe SQS and various short-distance bond lengths in the SQS as functions of x_{PbTe}, respectively. From Fig. 4 we see that average lattice parameter of PbS–PbTe solid solutions tends to be a composition-weighted average of the lattice parameters of PbS and PbTe, in agreement with Vegard's law.[83] Figure 5 highlights several points relevant to the observed low-T phase transitions in this alloy: (i) on average, the Pb–S and Pb–Te NN bonds retain lengths close to those of the constituent PbS and PbTe compounds, however (ii) there is considerable spread in the Pb–S bond lengths (as indicated by vertical bars in Fig. 5), especially compared to the Pb–Te bond lengths. (iii) The average cation–cation and anion–anion bond lengths are identical and follow Vegard's law similarly to the lattice parameters shown in Fig. 4,

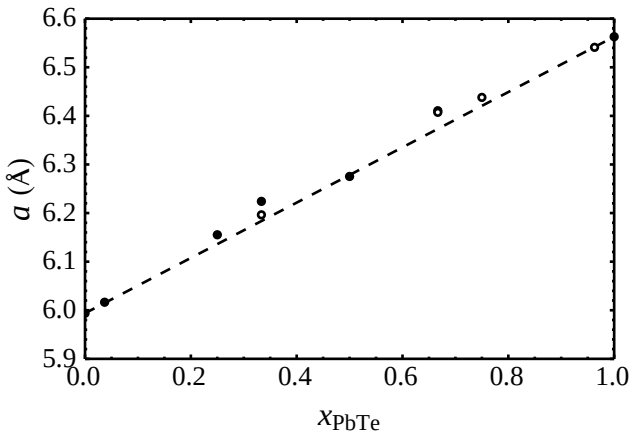

FIG. 4. Volume-averaged lattice parameters of PbS–PbTe SQS as a function of x_{PbTe}. Rocksalt lattice parameters are calculated for each SQS by taking $\sqrt[3]{8V_{\mathrm{SQS}}}$, where V_{SQS} is the volume-per-atom of an SQS. Solid circles show lattice parameters for SQS fully relaxed to their energy minima, while open circles show lattice parameters for SQS at saddle-points in their energy landscape. The dashed line is a linear interpolation between the lattice parameters of PbS and PbTe.

however, (iv) there is much more variation in the Pb–Pb bond lengths than the anion–anion bond lengths. This data suggests that the Pb and S ions are displaced significantly more from their ideal lattice sites than are the Te ions.

The calculated bond-length data are also in good agreement with experimental X-ray absorption fine structure (XAFS) measurements made at 30 K on PbS–PbTe alloys,[42] which show two distinct Pb–S bond lengths and one Pb–Te bond length (shown as blue and red squares in Fig. 5, respectively). The experimental Pb–S bond lengths lie within the standard deviations of Pb–S bond lengths of SQS with nearby compositions. The experimental Pb–Te bond lengths also lie within a standard deviation of the calculated Pb–Te average bond length.

To investigate these deviations in 1st and 2nd NN bond lengths from their ideal lengths in more detail, in Fig. 6 (a)–(d) we plot the distribution of Pb–S, Pb–Te, Pb–Pb, and anion–anion bonds for each PbS–PbTe SQS, respectively [panels (a) and (b) have the same horizontal plot range, as do panels (c) and (d)]. Bond-length distributions were obtained from the bond lengths of each SQS by fitting them to a Gaussian kernel.[84] The bond-length distributions for each SQS are shown off-set from one another along the y-axis for clarity, and distributions of structures fully relaxed to their minimum energy are shown as solid

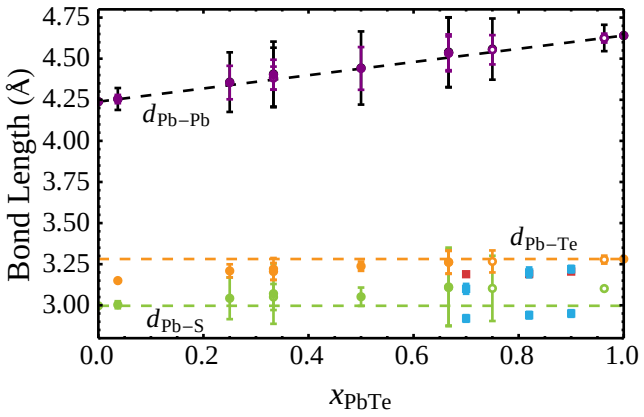

FIG. 5. (Color online) Average bond lengths in PbS–PbTe SQS as functions of the alloy composition, x_{PbTe}. Pb–S (green), Pb–Te (orange), Pb–Pb (black), and anion–anion (purple) bond lengths are shown, with average bond lengths of SQS at their energy minima shown as closed circles and average bond lengths of SQS at saddle-points shown as open circles. Vertical bars show the standard deviation of each average bond length. The green and orange dashed lines indicate $d_{\mathrm{Pb–S}}$ and $d_{\mathrm{Pb–Te}}$ in pure PbS and PbTe, respectively. The black dashed line indicates the composition-weighted average of $d_{\mathrm{Pb–Pb}}$ (and equivalently $d_{\mathrm{an–an}}$) for PbS and PbTe. The variance in $d_{\mathrm{Pb–S}}$ and $d_{\mathrm{Pb–Pb}}$ are much greater than the variance in $d_{\mathrm{Pb–Te}}$ and $d_{\mathrm{an–an}}$. Experimental data for Pb–S and Pb–Te bond lengths at 30 K from Ref. 42 are shown as blue and red squares, respectively.

lines while distributions of structures at saddle-points in their energy landscape are shown as dashed lines. For comparison, the corresponding bond lengths of bulk PbS and PbTe are shown in each panel of Fig. 6.

From Fig. 6 we can make several observations. First, the Pb–S and Pb–Te distributions are bimodal at concentrations close to $x_{\mathrm{PbTe}} = 0.5$, with the peaks in the Pb–S bond-length distribution occurring near the bulk PbS and PbTe bond lengths. Second, the Pb–Pb bond lengths are very broad, spanning a range of values from the bulk PbS Pb–Pb bond length to the bulk PbTe Pb–Pb bond length. Finally, while the anion–anion bond-length distributions are broader than the Pb–Te bond-length distributions, they are considerably more peaked than the Pb–Pb distributions, and their peaks follow the composition-weighted average of the S–S and Te–Te bond lengths of PbS and PbTe. From this data we conclude that the large lattice mismatch between PbS and PbTe is accommodated in the solid solution by

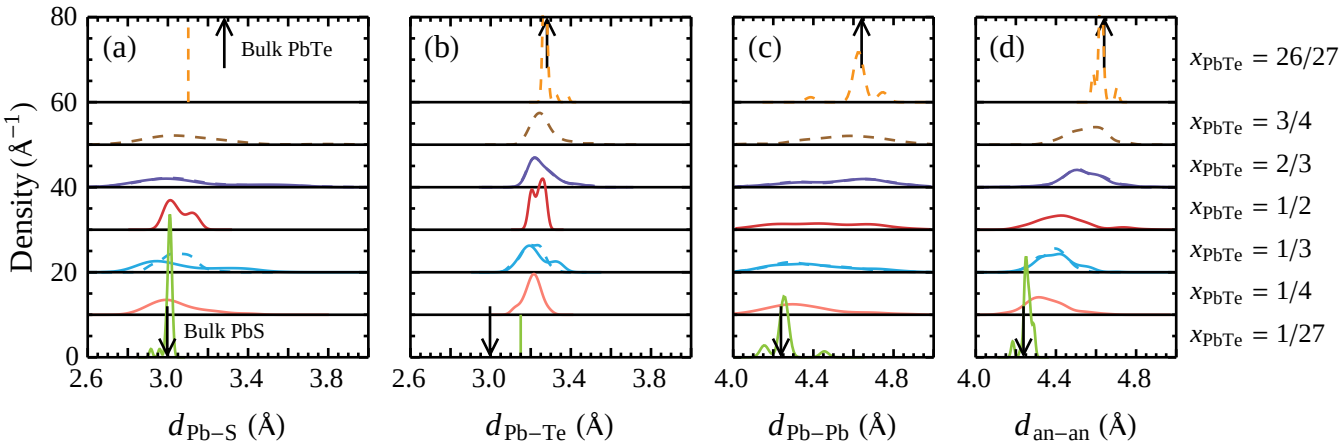

FIG. 6. (Color online) Distribution of bond lengths in PbS–PbTe SQS. Bond lengths shown are 1NN (a) Pb–S ($d_{\mathrm{Pb–S}}$) and (b) Pb–Te ($d_{\mathrm{Pb–Te}}$) bonds, and 2NN (c) Pb–Pb ($d_{\mathrm{Pb–Pb}}$) and (d) anion–anion ($d_{\mathrm{an–an}}$) bonds. Bond-length distributions of SQS in their energy minima are shown as solid lines and bond-length distributions of SQS at saddle-points in their energy landscapes are shown as dashed lines. Arrows indicate the corresponding bond lengths in bulk PbS and PbTe. Distributions are offset along the y-axis for clarity (with corresponding x-axes shows as horizontal dashed lines).

distortions of the Pb cation sublattice, with some smaller distortions of the S ions as well.

D. Low-T phase transitions

The low-energy double-well potentials of the PbS–PbTe SQS shown in Fig. 1 provide support for the idea that there exists a phase transition in these alloys at low temperatures: the double-well structures of the energy landscapes suggest a Landau-type phase transition[67,70] may be occurring, similar to displacive ferroelectric phase transitions in other IV–VI compounds and alloys such as SnTe,[85,86] GeTe,[87,88] PbTe–SnTe,[89] SnTe-GeTe,[90] and PbTe–GeTe.[91–93] The imaginary, or 'soft,' modes correspond primarily to displacements of S ions suggesting that the phase transition is due to the off-centering of these ions, as has been observed in the alkali-halides[43,44,94] and has been suggested to be the cause of the observed low-temperature behavior in PbS–PbTe alloys.[38–42]

We use our calculated phonon normal-mode frequencies in both the stable, 'well-bottom' configuration and the unstable 'saddle-point' configuration of the $x_{\mathrm{PbTe}} = 1/3$ and $x_{\mathrm{PbTe}} = 2/3$ SQS to model low temperature behavior of the PbS–PbTe alloys, following Ref. 67, as

discussed in Sec. II D. We determine anharmonic coupling constants between the phonon modes of the 'well-bottom' and 'saddle-point' configurations via Eq. (15). These anharmonic coupling constants are used to obtain a set of renormalized phonon frequencies for the low-T phase which depend on the magnitude of the unstable mode displacement, ϕ, as in Eq. (13). Using these renormalized phonon frequencies, we minimize the vibrational free energy of the system F [Eq. (16)] with respect to ϕ as a function of T to determine the equilibrium values of the soft-mode displacement as a function of temperature and find the transition temperature T_c where ϕ goes to zero.

In Fig. 7, we show the free energy in Eq. (16) as $\Delta F(\phi, T) = F(\phi, T) - F(0, T)$ as a function of ϕ at various temperatures for the (a) $x_{\mathrm{PbTe}} = 1/3$ and (b) $x_{\mathrm{PbTe}} = 2/3$ PbS–PbTe SQS. Closed circles connected by dashed lines indicate the values of ϕ that minimize the free energy at each temperature. Insets in each panel of Fig. 7 show the minimum-free-energy values of ϕ as functions of temperature, with dashed vertical lines indicating the T at which $\phi = 0$. By the construction of the model, the phase transitions in Fig. 7 are continuous,[67] with critical transition temperatures, T_c, of 46 K for $x_{\mathrm{PbTe}} = 1/3$ and 104 K for $x_{\mathrm{PbTe}} = 2/3$. The calculated transition temperatures are compared with experimentally observed transition temperatures in Sec. III E.

E. PbS–PbTe phase diagram

In Sec. III B we quantified the contributions to the free energy of mixing in PbS–PbTe solid solutions at high temperatures, and in Sec. III D we semi-quantitatively modeled the low-temperature displacive behavior of S ions in PbS–PbTe solid solutions. In this section, we construct the high- and low-temperature phase diagrams of PbS–PbTe based on these free energies and compare them to experimental data. Using Eqs. (6) and (7) we construct a miscibility gap for PbS–PbTe from ΔF_{mix}, shown in Fig. 3. This calculated miscibility gap is shown as a solid black line in Fig. 8. Using Eq. (7) we also calculate miscibility gaps corresponding to the bounds of the 90% confidence interval of Fig. 3, which is shown as a shaded region in Fig. 8. In Fig. 8 we also show a previously calculated miscibility gap for PbS–PbTe that neglects $\Delta S^{\mathrm{vib}}_{\mathrm{mix}}$ as a dashed, blue line.[14] Experimental data for the miscibility gap of PbS–PbTe are shown as open[11] and closed[12] circles. Our calculated low-T phase-transition temperatures for PbS–PbTe with compositions $x_{\mathrm{PbTe}} = 1/3$ and 2/3 are

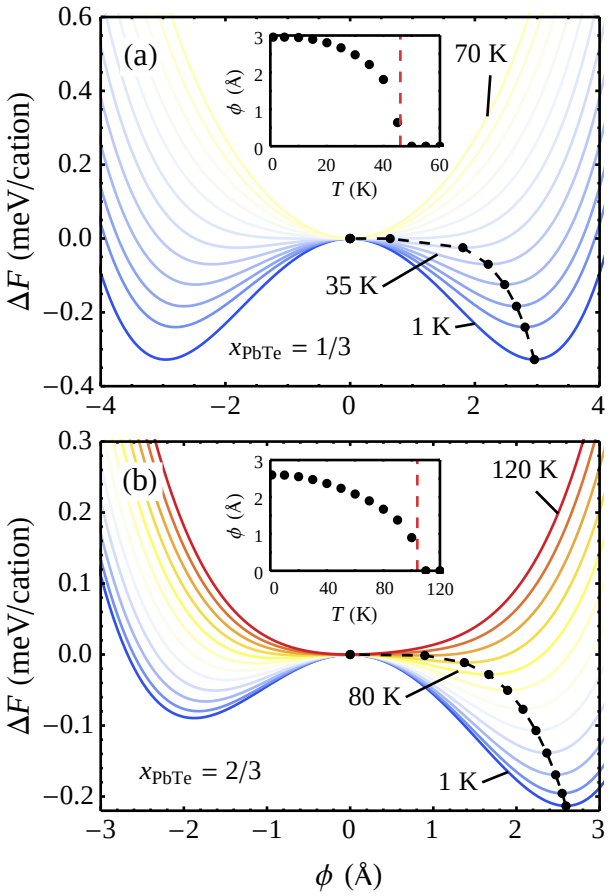

FIG. 7. (Color online) Difference in free energy between $F(\phi, T)$ and $F(0, T)$ as a function of ϕ at various T between (a) 0 and 60 K for $x_{\mathrm{PbTe}} = 1/3$ and (b) 0 and 120 K for $x_{\mathrm{PbTe}} = 2/3$. Closed circles connected by dashed lines indicate the values of ϕ which minimize $F(\phi, T)$ at each T. Insets in each panel show $\phi(T)$ as closed circles and T_c as vertical dashed lines for each system.

shown as red squares in Fig. 8. Finally, experimental data for low-T phase transitions in PbTe-rich PbS–PbTe alloys are shown as open squares in Fig. 8.[38]

Our calculated miscibility gap has a maximum temperature T_G of 1300 K, 470 K lower than the previously calculated T_G (without vibrational contributions) of 1770 K.[14] Both of these temperatures are higher than the experimental T_G which is 1070 K.[11,12] However, we see that the effect of the vibrational entropy of mixing in PbS–PbTe is to stabilize the solid solution relative to phase-separated PbS and PbTe, lowering the miscibility gap temperatures and improving the agreement of our calculated values to experiment. Our calculated low-T soft-mode phase-transition temperatures of 46 and 104 K compare favorably with the experimentally measured temperatures, which show a maximum T_c of 92 K at x_{PbTe} of 0.8.

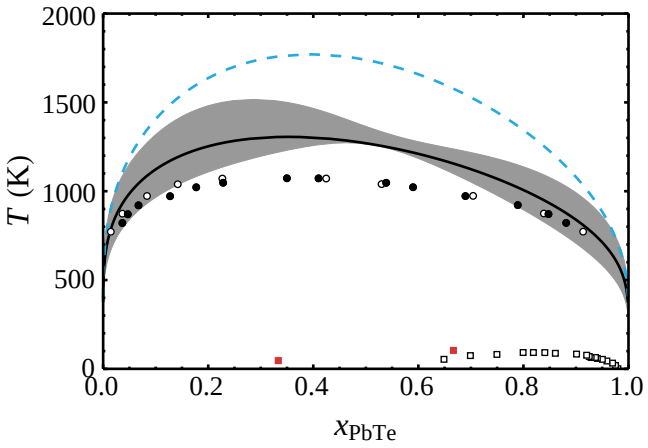

FIG. 8. (Color online) Calculated high- and low-T solid-state phase diagrams of PbS–PbTe. The solid black line shows the miscibility gap calculated using Eq. (6), with gaps calculated from the 90% confidence interval of the free energy fit shown as the gray shaded region. The dashed blue line shows a previously calculated miscibility gap for PbS–PbTe that neglects $\Delta S^{\text{vib}}_{\text{mix}}$.[14] Red squares show calculated low-T phase transition temperatures. Open[11] and closed[12] circles show the experimentally measured miscibility gap of PbS–PbTe, and open squares[38] show the experimentally measured low-T phase transition temperatures of PbS–PbTe.

The experimental work only investigated PbTe-rich compositions, however our calculations predict the existence of low-T phase transitions at PbS-rich compositions as well.

IV. CONCLUSIONS

In this work, we used first-principles DFT calculations to investigate the role that vibrations play in the thermodynamics of PbS–PbTe alloys. We used special quasirandom structures (SQS) to approximate the atomic structure of the solid solution of PbS–PbTe alloys. These SQS were then relaxed within DFT and their vibrational spectra were calculated with the frozen-phonon method. We found that several of these SQS had relaxed to saddle points in their energy landscapes, leading to unstable phonon modes with double-well energy vs. phonon mode displacement curves. These phonon modes corresponded to motion of S ions within the rocksalt lattice, providing theoretical support for the experimental observations of phase transitions in PbS–PbTe alloys at low temperatures. In addition to the dynamic displacements of S ions, structural analysis of the PbS–PbTe SQS showed that

the Pb cations are statically displaced from their ideal lattice sites due to the size mismatch between PbS and PbTe. These observations may relate to the proposed off-centering of Pb ions in pure PbS and PbTe with increasing T,[27,29,31,34] though anharmonic effects seem to account for the experimentally observed phenomena in the pure compounds.[28,35,36]

From the calculated vibrational spectra of dynamically stable PbS–PbTe SQS we obtained phonon DOSs and used them to determine the high-temperature vibrational entropy of mixing in PbS–PbTe solid solutions. We combined these entropies with the zero Kelvin SQS mixing energies to obtain the Helmholtz free energy of mixing for PbS–PbTe. We used this free energy to calculate the solid-solid phase diagram for PbS–PbTe, which we found to have a miscibility gap in agreement with experiment. We found that the inclusion of the vibrational entropy of mixing in the free energy brought the calculated miscibility gap into better agreement with experiment. We also used the calculated vibrational spectra of the SQS at $x_{\mathrm{PbTe}} = 1/3$ and $2/3$ to determine low-T displacive phase transition temperatures, which we found to be in good qualitative agreement with experimental data at compositions near $x_{\mathrm{PbTe}} = 1/3$. Based on our calculation of a transition at $x_{\mathrm{PbTe}} = 2/3$, we predict that PbS–PbTe alloys should undergo displacive phase transitions at PbS-rich compositions as well. We find the vibrational properties of PbS–PbTe alloys to play an important role in the thermodynamics of these materials, and their inclusion in the free energy of mixing is crucial to a quantitative description of the phase transitions in these alloys.

ACKNOWLEDGMENTS

The authors acknowledge financial support from the U.S. Department of Energy under grant DE-FG02-07ER46433. This research used resources of the National Energy Research Scientific Computing Center, a DOE Office of Science User Facility supported by the Office of Science of the U.S. Department of Energy under Contract No. DE-AC02-05CH11231, as well as the Northwestern University Quest computing resources. The figures for this article have been created using the LevelScheme scientific figure preparation system.[95]

TABLE IV. Description of the 27-atom SQS supercells for $x = 1/3$ and $x = 2/3$.

SQS-27 ($x = 1/3$)		A_3BC_2
	Lattice vectors	
$a_1 = (0.0, 1.5, 1.5)$	$a_2 = (1.5, 0.0, 1.5)$	$a_3 = (1.5, 1.5, 0.0)$
	Atomic Positions	
fcc-mixing atoms		rocksalt spectator cation atoms
B—$(0.0, 0.0, 0.0)$		A—$(0.5, 0.5, 0.5)$
B—$(0.0, 0.5, 0.5)$		A—$(0.5, 1.0, 1.0)$
B—$(0.0, -0.5, -0.5)$		A—$(0.5, 0.0, 0.0)$
B—$(0.5, 0.0, 0.5)$		A—$(1.0, 0.5, 1.0)$
B—$(-0.5, 0.5, 0.0)$		A—$(0.0, 1.0, 0.0)$
B—$(-0.5, 0.5, -1.0)$		A—$(0.0, 1.0, -0.5)$
B—$(-0.5, 0.0, 0.5)$		A—$(0.0, 0.5, 1.0)$
B—$(0.0, -0.5, 0.5)$		A—$(0.5, 0.0, 1.0)$
B—$(0.5, 0.5, -1.0)$		A—$(1.0, 1.0, -0.5)$
C—$(0.5, -1.0, -0.5)$		A—$(1.0, -0.5, 0.0)$
C—$(0.5, -0.5, 0.0)$		A—$(1.0, 0.0, 0.5)$
C—$(-0.5, 0.0, -0.5)$		A—$(0.0, 0.5, 0.0)$
C—$(-0.5, -0.5, -1.0)$		A—$(0.0, 0.0, -0.5)$
C—$(0.5, 0.5, 0.0)$		A—$(1.0, 1.0, 0.5)$
C—$(0.5, -0.5, -1.0)$		A—$(1.0, 0.0, -0.5)$
C—$(0.5, 0.0, -0.5)$		A—$(1.0, 0.5, 0.0)$
C—$(1.0, -0.5, -0.5)$		A—$(1.5, 0.0, 0.0)$
C—$(1.0, 0.0, 0.0)$		A—$(1.5, 0.5, 0.5)$
C—$(0.0, 0.5, -0.5)$		A—$(0.5, 1.0, 0.0)$
C—$(0.0, 1.0, 0.0)$		A—$(0.5, 1.5, 0.5)$
C—$(0.0, 0.0, -1.0)$		A—$(0.5, 0.5, -0.5)$
C—$(-0.5, -0.5, 0.0)$		A—$(0.0, 0.0, 0.5)$
C—$(-0.5, -1.0, -0.5)$		A—$(0.0, -0.5, 0.0)$
C—$(0.0, 0.0, 1.0)$		A—$(0.5, 0.5, 1.5)$
C—$(0.0, -1.0, 0.0)$		A—$(0.5, -0.5, 0.5)$
C—$(-1.0, -0.5, -0.5)$		A—$(-0.5, 0.0, 0.0)$
C—$(-1.0, 0.0, 0.0)$		A—$(-0.5, 0.5, 0.5)$

Appendix A: Description of 27-atom SQS

Table IV contains the unit-cell parameters and atomic positions of the mixing atoms for the fcc SQS-27 supercells, as well as the atomic positions of the spectator cation atoms for the rocksalt SQS-54 supercells at a composition of $x = 1/3$. The structure for $x = 2/3$ can be obtained by switching B and C atoms. Table V contains local composition and geometric information for each Pb cation in the PbS–PbTe SQS in their low-T, well-bottom configurations and/or high-T saddle-point configurations.

TABLE V. Composition and geometry of Pb NN coordination. For each SQS, the number of Pb ions with 0–6 Pb–Te NN bonds are reported along with statistics of Pb–S and Pb–Te bond lengths for Pb ions with that Te coordination. Numbers listed without standard deviations are either single bond lengths or bond lengths equivalent by symmetry.

System	# Pb–Te NN Bonds						
	0	1	2	3	4	5	6
$x_{\mathrm{PbTe}} = 1/27$							
# Pb ions	21	6					
$\langle d_{\mathrm{Pb–S}} \rangle$ (Å)	3.004 ± 0.012	3.000 ± 0.042					
$\langle d_{\mathrm{Pb–Te}} \rangle$ (Å)		3.150					
$x_{\mathrm{PbTe}} = 1/4$							
# Pb ions	4	3	6	3			
$\langle d_{\mathrm{Pb–S}} \rangle$ (Å)	3.038 ± 0.087	3.050 ± 0.128	3.042 ± 0.143	3.045 ± 0.163			
$\langle d_{\mathrm{Pb–Te}} \rangle$ (Å)		3.182 ± 0.041	3.220 ± 0.042	3.204 ± 0.030			
$x_{\mathrm{PbTe}} = 1/3$ well							
# Pb ions	2	8	8	7	1	1	
$\langle d_{\mathrm{Pb–S}} \rangle$ (Å)	3.056 ± 0.127	3.075 ± 0.191	3.073 ± 0.188	3.084 ± 0.196	2.950 ± 0.023	2.962	
$\langle d_{\mathrm{Pb–Te}} \rangle$ (Å)		3.267 ± 0.072	3.225 ± 0.060	3.207 ± 0.061	3.196 ± 0.062	3.219 ± 0.067	
$x_{\mathrm{PbTe}} = 1/3$ saddle-point							
# Pb ions	2	8	8	7	1	1	
$\langle d_{\mathrm{Pb–S}} \rangle$ (Å)	3.046 ± 0.027	3.056 ± 0.071	3.049 ± 0.079	3.060 ± 0.103	2.921 ± 0.006	2.966	
$\langle d_{\mathrm{Pb–Te}} \rangle$ (Å)		3.241 ± 0.034	3.210 ± 0.036	3.193 ± 0.054	3.186 ± 0.069	3.201 ± 0.062	
$x_{\mathrm{PbTe}} = 1/2$							
# Pb ions		2	4	4	4	2	
$\langle d_{\mathrm{Pb–S}} \rangle$ (Å)		3.050 ± 0.054	3.036 ± 0.060	3.048 ± 0.047	3.090 ± 0.052	3.059	
$\langle d_{\mathrm{Pb–Te}} \rangle$ (Å)		3.211	3.248 ± 0.018	3.238 ± 0.033	3.233 ± 0.027	3.243 ± 0.029	
$x_{\mathrm{PbTe}} = 2/3$ well							
# Pb ions		1	1	7	8	8	2
$\langle d_{\mathrm{Pb–S}} \rangle$ (Å)		3.141 ± 0.262	3.070 ± 0.333	3.115 ± 0.263	3.137 ± 0.208	3.055 ± 0.119	
$\langle d_{\mathrm{Pb–Te}} \rangle$ (Å)		3.260	3.438 ± 0.018	3.277 ± 0.065	3.260 ± 0.073	3.253 ± 0.062	3.243 ± 0.035
$x_{\mathrm{PbTe}} = 2/3$ saddle-point							
# Pb ions		1	1	7	8	8	2
$\langle d_{\mathrm{Pb–S}} \rangle$ (Å)		3.107 ± 0.182	3.073 ± 0.316	3.111 ± 0.246	3.144 ± 0.235	3.045 ± 0.113	
$\langle d_{\mathrm{Pb–Te}} \rangle$ (Å)		3.266	3.455 ± 0.038	3.275 ± 0.070	3.260 ± 0.073	3.253 ± 0.065	3.242 ± 0.039
$x_{\mathrm{PbTe}} = 3/4$ saddle-point							
# Pb ions				3	6	3	4
$\langle d_{\mathrm{Pb–S}} \rangle$ (Å)				3.139 ± 0.278	3.077 ± 0.118	3.098 ± 0.147	
$\langle d_{\mathrm{Pb–Te}} \rangle$ (Å)				3.266 ± 0.095	3.283 ± 0.074	3.264 ± 0.067	3.253 ± 0.037
$x_{\mathrm{PbTe}} = 26/27$ saddle-point							
# Pb ions						6	21
$\langle d_{\mathrm{Pb–S}} \rangle$ (Å)						3.102	
$\langle d_{\mathrm{Pb–Te}} \rangle$ (Å)						3.292 ± 0.046	3.274 ± 0.013

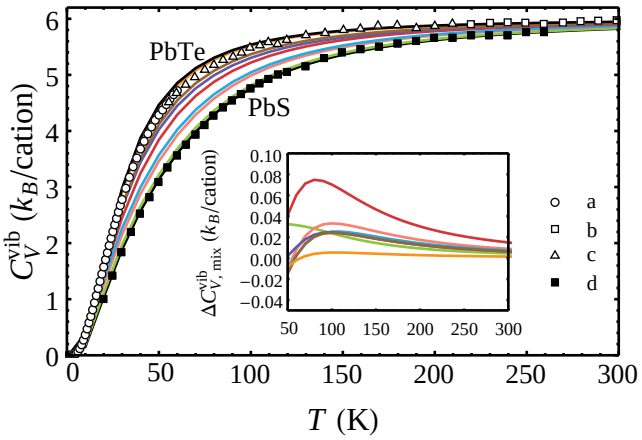

FIG. 9. (Color online) Calculated and measured heat capacity (at constant volume) of PbS–PbTe alloys as functions of temperature. Curves show calculated heat capacities. Open and closed points show experimental heat capacities of PbTe and Pbs, respectively. The inset panel shows the calculated heat capacities of mixing for PbS–PbTe alloys. The heat capacities approach zero around room temperature. Experimental data for PbTe were converted from C_P to C_V using the thermal expansion and bulk modulus data of Ref. 96. Experimental data: a – Ref. 97, b – Ref. 98, c – Ref. 99, d – Ref. 100.

Appendix B: Heat capacity of PbS–PbTe alloys

Figure 9 shows both calculated and experimental heat capacites at constant volume for the PbS–PbTe alloys. Calculated heat capacities are shown as solid lines and experimental heat capacities as points. The calculated heat capacities for PbTe and PbS (black, solid lines in Fig. 9) are in good agreement with the experimentally measured heat capacities. The heat capacities of the PbS–PbTe alloys all lie within the heat capacities of PbTe and PbS. The inset of Fig. 9 shows the heat capacities of mixing, defined by

$$\Delta C_{V,\rm mix}^{\rm vib}(x,T) = C_V^{\rm vib}(x,T) - (1-x)C_V^{\rm vib}({\rm PbS},T) - xC_V^{\rm vib}({\rm PbTe},T), \qquad \text{(B1)}$$

where $C_V^{\rm vib}(x,T)$ is the heat capacity of an alloy with composition x, $C_V^{\rm vib}({\rm PbS},T)$ is the heat capacity of PbS, and $C_V^{\rm vib}({\rm PbTe},T)$ is the heat capacity of PbTe. The heat capacities of mixing for PbS–PbTe are all very small and decrease with increasing temperature, approaching zero around room temperature. This negligible heat capacity of mixing gives credence to the use of Eq. (10).

* c-wolverton@northwestern.edu

[1] J. Androulakis, C.-H. Lin, H.-J. Kong, C. Uher, C.-I. Wu, T. Hogan, B. A. Cook, T. Caillat, K. M. Paraskevopoulos, and M. G. Kanatzidis, J. Am. Chem. Soc. **129**, 9780 (2007).

[2] J. Androulakis, I. Todorov, J. He, D.-Y. Chung, V. Dravid, and M. Kanatzidis, J. Am. Chem. Soc. **133**, 10920 (2011).

[3] K. Biswas, J. He, Q. Zhang, G. Wang, C. Uher, V. P. Dravid, and M. G. Kanatzidis, Nat. Chem. **3**, 160 (2011).

[4] K. Biswas, J. He, I. D. Blum, C.-I. Wu, T. P. Hogan, D. N. Seidman, V. P. Dravid, and M. G. Kanatzidis, Nature **489**, 414 (2012).

[5] L.-D. Zhao, S. Hao, S.-H. Lo, C.-I. Wu, X. Zhou, Y. Lee, H. Li, K. Biswas, T. P. Hogan, C. Uher, C. Wolverton, V. P. Dravid, and M. G. Kanatzidis, J. Am. Chem. Soc. **135**, 7364 (2013).

[6] R. J. Korkosz, T. C. Chasapis, S.-H. Lo, J. W. Doak, Y. J. Kim, C.-I. Wu, E. Hatzikraniotis, T. P. Hogan, D. N. Seidman, C. Wolverton, V. P. Dravid, and M. G. Kanatzidis, J. Am. Chem. Soc. **136**, 3225 (2014).

[7] G. Tan, L.-D. Zhao, F. Shi, J. W. Doak, S.-H. Lo, H. Sun, C. Wolverton, V. P. Dravid, C. Uher, and M. G. Kanatzidis, J. Am. Chem. Soc. **136**, 7006 (2014).

[8] G. Tan, F. Shi, J. W. Doak, H. Sun, L.-D. Zhao, P. Wang, C. Uher, C. Wolverton, V. P. Dravid, and M. G. Kanatzidis, Energy Environ. Sci. **8**, 267 (2015).

[9] J. He, S. N. Girard, M. G. Kanatzidis, and V. P. Dravid, Adv. Funct. Mater. **20**, 764 (2010).

[10] S. N. Girard, J. He, V. P. Dravid, and M. G. Kanatzidis, in *Mater. Res. Soc. Symp. Proc.*, Vol. 1267 (2010) pp. 2–7.

[11] M. S. Darrow, W. B. White, and R. Roy, Trans. Metall. Soc. AIME **236**, 654 (1966).

[12] V. Leute and N. Volkmer, Z. Phys. Chem. **144**, 145 (1985).

[13] H. Lin, E. S. Božin, S. J. L. Billinge, J. Androulakis, C. D. Malliakas, C. H. Lin, and M. G. Kanatzidis, Phys. Rev. B **80**, 045204 (2009).

[14] J. W. Doak and C. Wolverton, Phys. Rev. B **86**, 144202 (2012).

[15] Y. Wang, S. L. Shang, L. Q. Chen, and Z. K. Liu, Int. J. Quantum Chem. **111**, 3565 (2011).

[16] C. Wolverton and A. Zunger, Phys. Rev. B **52**, 8813 (1995).

[17] V. Ozoliņš, C. Wolverton, and A. Zunger, Phys. Rev. B **57**, 6427 (1998).

[18] V. Ozoliņš and M. Asta, Phys. Rev. Lett. **86**, 448 (2001).

[19] D. de Fontaine, Solid State Phys. **34**, 73 (1979).

[20] V. Ozoliņš, C. Wolverton, and A. Zunger, Phys. Rev. B **58**, 5897 (1998).

[21] D. Morgan, A. van de Walle, G. Ceder, J. D. Althoff, and D. de Fontaine, Model. Simul. Mater. Sci. Eng. **8**, 295 (2000).

[22] M. Asta and V. Ozoliņš, Phys. Rev. B **64**, 094104 (2001).

[23] A. van de Walle and G. Ceder, Rev. Mod. Phys. **74**, 11 (2002).

[24] B. Fultz, Prog. Mater. Sci. **55**, 247 (2010).

[25] R. Dalvin, Solid State Phys. **28**, 179 (1973).

[26] M. L. Cohen and J. R. Chelikowsky, *Electronic Structure and Optical Properties of Semiconductors* (Springer-Verlag, Berlin, 1989).

[27] E. S. Božin, C. D. Malliakas, P. Souvatzis, T. Proffen, N. A. Spaldin, M. G. Kanatzidis, and S. J. L. Billinge, Science **330**, 1660 (2010).

[28] O. Delaire, J. Ma, K. Marty, A. F. May, M. A. McGuire, M.-H. Du, D. J. Singh, A. Podlesnyak, G. Ehlers, M. D. Lumsden, and B. C. Sales, Nat. Mater. **10**, 614 (2011).

[29] Y. Zhang, X. Ke, P. R. C. Kent, J. Yang, and C. Chen, Phys. Rev. Lett. **107**, 175503 (2011).

[30] H. Kim and M. Kaviany, Phys. Rev. B **86**, 045213 (2012).

[31] K. M. Ø. Jensen, E. S. Božin, C. D. Malliakas, M. B. Stone, M. D. Lumsden, M. G. Kanatzidis, S. M. Shapiro, and S. J. L. Billinge, Phys. Rev. B **86**, 085313 (2012).

[32] T. Shiga, J. Shiomi, J. Ma, O. Delaire, T. Radzynski, A. Lusakowski, K. Esfarjani, and G. Chen, Phys. Rev. B **85**, 155203 (2012).

[33] T. Keiber, F. Bridges, and B. C. Sales, Phys. Rev. Lett. **111**, 095504 (2013).

[34] S. Kastbjerg, N. Bindzus, M. Søndergaard, S. Johnsen, N. Lock, M. Christensen, M. Takata, M. A. Spackman, and B. B. Iversen, Adv. Funct. Mater. **23**, 5477 (2013).

[35] C. W. Li, O. Hellman, J. Ma, A. F. May, H. B. Cao, X. Chen, A. D. Christianson, G. Ehlers, D. J. Singh, B. C. Sales, and O. Delaire, Phys. Rev. Lett. **112**, 175501 (2014).

[36] C. W. Li, J. Ma, H. B. Cao, A. F. May, D. L. Abernathy, G. Ehlers, C. Hoffmann, X. Wang, T. Hong, A. Huq, O. Gourdon, and O. Delaire, Phys. Rev. B **90**, 214303 (2014).

[37] P. B. Littlewood, J. Phys. C **13**, 4855 (1980).

[38] K. A. Abdullin, A. I. Lebedev, A. M. Gas'kov, V. N. Demin, and V. P. Zlomanov, JEPT Lett. **40**, 998 (1984).

[39] K. A. Abdullin, V. N. Demin, and A. I. Lebedev, Sov. Phys. Solid State **28**, 570 (1986).

[40] A. I. Dmitriev, G. V. Lashkarev, V. I. Litvinov, A. M. Gas'kov, and V. N. Demin, JEPT Lett. **45**, 383 (1987).

[41] A. I. Dmitriev, V. I. Lazorenko, V. I. Litvinov, and G. V. Lashkarev, JEPT Lett. **47**, 669 (1988).

[42] Z. Wang and B. A. Bunker, Phys. Rev. B **46**, 11277 (1992).

[43] G. Lombardo and R. O. Pohl, Phys. Rev. Lett. **15**, 291 (1965).

[44] H. S. Sack and M. C. Moriarty, Solid State Commun. **3**, 93 (1965).

[45] B. E. Vugmeister and M. D. Glinchuk, Rev. Mod. Phys. **62**, 993 (1990).

[46] A. A. Bokov and Z.-G. Ye, J. Mater. Sci. **41**, 31 (2006).

[47] P. Hohenberg and W. Kohn, Phys. Rev. **136**, B864 (1964).

[48] W. Kohn and L. J. Sham, Phys. Rev. **140**, A1133 (1965).

[49] A. Zunger, S.-H. Wei, L. G. Ferreira, and J. E. Bernard, Phys. Rev. Lett. **65**, 353 (1990).

[50] S.-H. Wei, L. G. Ferreira, J. E. Bernard, and A. Zunger, Phys. Rev. B **42**, 9622 (1990).

[51] J. An, A. Subedi, and D. J. Singh, Solid State Commun. **148**, 417 (2008).

[52] Y. Zhang, X. Ke, C. Chen, J. Yang, and P. R. C. Kent, Phys. Rev. B **80**, 024304 (2009).

[53] M. D. Nielsen, V. Ozoliņš, and J. P. Heremans, Energy Environ. Sci. **6**, 570 (2013).

[54] J. M. Skelton, S. C. Parker, A. Togo, I. Tanaka, and A. Walsh, Phys. Rev. B **89**, 205203 (2014).

[55] Y. Chen, X. Ai, and C. A. Marianetti, Phys. Rev. Lett. **113**, 105501 (2014).

[56] S.-H. Wei and A. Zunger, Phys. Rev. B **55**, 13605 (1997).

[57] S. V. Barabash, V. Ozoliņš, and C. Wolverton, Phys. Rev. Lett. **101**, 155704 (2008).

[58] S. V. Barabash, V. Ozoliņš, and C. Wolverton, Phys. Rev. B **78**, 214109 (2008).

[59] S. V. Barabash and V. Ozoliņš, Phys. Rev. B **81**, 075212 (2010).

[60] S. Hao, L.-D. Zhao, C.-Q. Chen, V. P. Dravid, M. G. Kanatzidis, and C. M. Wolverton, J. Am. Chem. Soc. **136**, 1628 (2014).

[61] C. Wolverton and A. Zunger, Comput. Mater. Sci. **8**, 107 (1997).

[62] S. Müller, L.-W. Wang, A. Zunger, and C. Wolverton, Phys. Rev. B **60**, 16448 (1999).

[63] J. Z. Liu and A. Zunger, Phys. Rev. B **77**, 205201 (2008).

[64] B. P. Burton and A. van de Walle, Chem. Geol. **225**, 222 (2006).

[65] C. K. Gan, Y. P. Feng, and D. J. Srolovitz, Phys. Rev. B **73**, 235214 (2006).

[66] C. K. Gan, X. F. Fan, and J.-L. Kuo, Comput. Mater. Sci. **49**, S29 (2010).

[67] M. T. Dove, A. P. Giddy, and V. Heine, Ferroelectrics **136**, 33 (1992).

[68] C. Wolverton, Acta Mater. **49**, 3129 (2001).

[69] O. Redlich and A. T. Kister, Ind. Eng. Chem. **40**, 345 (1948).

[70] M. T. Dove, *Introduction to Lattice Dynamics* (Cambridge University Press, New York, 1993).

[71] G. Kresse and J. Hafner, Phys. Rev. B **47**, 558 (1993).

[72] G. Kresse and J. Hafner, Phys. Rev. B **49**, 14251 (1994).

[73] G. Kresse and J. Furthmüller, Phys. Rev. B **54**, 11169 (1996).

[74] G. Kresse and J. Furthmüller, Comput. Mater. Sci. **6**, 15 (1996).

[75] P. E. Blöchl, Phys. Rev. B **50**, 17953 (1994).

[76] G. Kresse and D. Joubert, Phys. Rev. B **59**, 1758 (1999).

[77] J. P. Perdew, K. Burke, and M. Ernzerhof, Phys. Rev. Lett. **77**, 3865 (1996).

[78] H. J. Monkhorst and J. D. Pack, Phys. Rev. B **13**, 5188 (1976).

[79] P. Pulay, Chem. Phys. Lett. **73**, 393 (1980).

[80] C. Wolverton, V. Ozoliņš, and M. Asta, Phys. Rev. B **69**, 144109 (2004).

[81] W. Cochran, R. A. Cowley, G. Dolling, and M. M. Elcombe, Proc. R. Soc. London, Ser. A **293**, 433 (1966).

[82] M. M. Elcombe, Proc. R. Soc. London, Ser. A **300**, 210 (1967).

[83] L. Vegard, Z. Phys. **5**, 17 (1921).

[84] D. W. Scott, *Multivariate Density Estimation: Theory, Practice, and Visualization* (John Wiley and Sons, Inc., New York, 1992).

[85] S. Sugai, K. Murase, and H. Kawamura, Solid State Commun. **23**, 127 (1977).

[86] S. Sugai, K. Murase, S. Katayama, S. Takaoka, S. Nishi, and H. Kawamura, Solid State Commun. **24**, 407 (1977).

[87] E. F. Steigmeier and G. Harbeke, Solid State Commun. **8**, 1275 (1970).

[88] K. M. Rabe and J. D. Joannopoulos, Phys. Rev. B **36**, 6631 (1987).

[89] G. Dolling and W. J. L. Buyers, J. Nonmetals **1**, 159 (1973).

[90] G. S. Pawley, W. Cochran, R. A. Cowley, and G. Dolling, Phys. Rev. Lett. **17**, 753 (1966).

[91] S. Sugai, K. Murase, T. Tsuchihira, and H. Kawamura, J. Phys. Soc. Japan **47**, 539 (1979).

[92] K. A. Abdullin and A. I. Lebedev, Sov. Phys. Solid State **25**, 2055 (1983).

[93] S. Takaoka and K. Murase, Phys. Rev. B **20**, 2823 (1979).

[94] B. Fischer and M. W. Klein, Phys. Rev. Lett. **37**, 756 (1976).

[95] M. A. Caprio, Comput. Phys. Commun. **171**, 107 (2005).

[96] B. Houston, R. E. Strakna, and H. S. Belson, J. Appl. Phys. **39**, 3913 (1968).

[97] A. J. Bevolo, H. R. Shanks, and D. E. Eckels, Phys. Rev. B **13**, 3523 (1976).

[98] A. S. Pashinkin, M. S. Mikhailova, A. S. Malkova, and V. A. Fedorov, Inorg. Mater. **45**, 1226 (2009).

[99] D. H. Parkinson and J. E. Quarrington, Proc. Phys. Soc. Sect. A **67**, 569 (1954).

[100] M. Cardona, R. K. Kremer, R. Lauck, G. Siegle, J. Serrano, and A. H. Romero, Phys. Rev. B **76**, 075211 (2007).